Robust supramolecular nano-tunnels built from molecular bricks

Peifa Wei,[1,2] Zheng Zheng,[1] Junyi Gong,[1] Jun Zhang,[1] Herman H.-Y. Sung,[1] Ian D. Williams,[1] Jacky W. Y. Lam,[1] & Ben Zhong Tang*[,1,3]

[1]Department of Chemistry, The Hong Kong Branch of Chinese National Engineering Research Center for Tissue Restoration and Reconstruction, Institute for Advanced Study, Department of Chemical and Biological Engineering, The Hong Kong University of Science and Technology, Clear Water Bay, Kowloon, Hong Kong, China

[2]Institutes of Physical Science and Information Technology, Anhui University, Hefei 230601, China

[3]Center for Aggregation-Induced Emission, SCUT-HKUST Joint Research Institute, State Key Laboratory of Luminescent Materials and Devices, South China University of Technology, Guangzhou, 510640, China

Abstract

Chemists are always seeking new methods to construct porous lattice frameworks using simple motifs as the impetus. Different from the extensively reported frameworks which were stabilized by extended bonding, porous crystals of discrete organic molecules is an emerging area of porous materials with dynamic and flexible conformation, consisting exclusively of non-covalent interactions. Herein we report geometrically simple linear molecule that assemble into a supramolecular nano-tunnel through synergy of anionic trident and multiple intermolecular π-π stacking interactions. The nano-tunnel crystal exhibit exceptional chemical stability in concentrated HCl and NaOH aqueous solutions, which is rarely been seen in supramolecular organic frameworks and often related to designed extensive hydrogen bonding interactions. Upon thermal treatment, the formed nano-tunnel crystals go through multistage single-crystal-to-single-crystal phase transformations accompanied by thermosalient effect. Aggregation-induced emission joins with the adaptive pores render the crystals with responsive fluorescent change from blue to yellow and visible self-healing porosity transformation upon being stimulated. Furthermore, the desolvated pores exhibit highly selective CO_2 adsorption at ambient temperature.

Introduction

Nature is unrivaled in its ability to create structural complexity from small organic molecules. Chemists have been also always pursing the virtues of simplicity in constructing functional structures using simple motifs, with the benefit of readily synthetic feasibility and more structural tunability.[1-3] Recently, an emerging area of porous materials is the study of porous crystals of discrete organic small molecules, consisting exclusively of non-covalent interactions.[4-8] Such organic molecular crystals can exhibit porosity that can compete with porous networks such as metal–organic and covalent organic frameworks.[9-11]

To obtain robust porous molecular crystals constructed using simple tectons relies on ingenious molecular design.[12] The topology of the tectons should geometrically favorable for the formation of stable framework with "vitual porosity" by maximum the interactions with minium the contact points. Up to now, the most common tectons in reported frameworks are predesigned three- or multi-armed scaffolds.[13,14] Linear two-armed tectons is easier to synthesize, but geometrically difficult to form architectures with open pores. Therefore, few supramolecular structure/material based on linear tectons has been reported so far.

On the other hand, the linkage interactions that strong enough to stabilize supramolecular frameworks are still limited. H-bonding is still the most common and most effective linkage to construct such frameworks. Among those H-bonded frameworks, a few examples, reported by Miljanić, Aida, Schröder and others, have shown good thermal and chemical stability. However, these systems are often required specific functional groups and can be labile to solvents that will interfere H-bonds.[15,16] Other interactions, such as π-π stacking and ionic interactions, has been explored recently as effective protocol that can strengthen the intermolecular interactions.[17] Here we reported that a simple linear molecule can be used to construct a robust framework with open pores. The linear tectons are firstly forming specific three-armed supramolecular synthons, which further assembling into stable framework through a combination of trident-type anionic interactions and π-π stacking interactions. Noteworthy, the linear cyanostilbene-based tecton is a readily accessible aggregation-induced emission (AIE) fluorophore which gives the framework luminescent in the solid state.[18] This inherent AIE feature, with high sensitivity and low background noise visualization signals, [19] is useful tool to monitor the variability of pores, for example, their fluorescent response when including guest molecules. The tunnel material has a visible self-healing behavior with on-off-on porosity transformation upon grinding and solvent-fuming. Rarely, this supramolecular tunnel shows good chemical stability and retain crystalline and porous at strong acid and base condition. The material also exhibit multistage polymorphic single-crystal-to-single-crystal phase transformations, accompanied by thermosalient effect, in response to thermal treatment. The formed porous structure has been proven very selective to CO_2 at room temperature.

Results

Paraquat is a well-known planar electron-acceptor and dicyanostilbene is an AIE fluorophore with twisted conformation. By combining these two units, we designed a new molecule, **PCS**, which is readily available in gram-scale quantities via a four-step synthetic method (Fig. 1a, Supplementary Figs. 1-4 and Scheme S1). The sharp single peak in as synthesised HPLC of **PCS** and identification of the *Z*-conformation only in the single crystal indicated that the *E*-isomer was not formed during the reaction. (Supplementary Figs. 5 and 6). The electrostatic potential (ESP) diagram (Supplementary Fig. 7a) of **PCS** shows that there are no electron rich parts in the structure. This further leads to weak intermolecular interactions, such as weak intermolecular π-π interactions, as confirmed by intermolecular independent gradient model (IGM) surface mapping (Supplementary Fig. 7b). The structure is linear with two crystallographically distinct arms. The four phenyl rings on the two arms twist in

different angles out of the plane of the central dicyanoethylene (Supplementary Fig. 6). The twisted conformation in association with intermolecular π-π interactions lead to inefficient molecular packing which can in principle fulfill the requirement of "point contact" for porous structure (Fig. 1h). Single-crystal X-ray diffraction reveals that one PF_6^- can act as a joint that interacts with up to five **PCS** molecules through multiple C-H…F and F…π ionic interactions with distance vary between 2.14 ~ 3.16 Å (Supplementary Fig. 8). Each PF_6^- counteranion acts as an anionic trident to connect three **PCS** at three adjacent layers to form a stable three-armed supramolecular synthon (Fig. 1h). The anionic trident has been seen to play a similar role as metal nodes in MOFs which can control the direction of supramolecular synthon. It should be noted that for the single crystal structure of **PCS** with I^- as counteranion, a dense packing without pore structure was observed which proved the contribution on the formation of open pores brought by PF_6^- (Supplementary Fig. 9). Two supramolecular synthons can pack in a brickwork type of arrangement to form dumbbell-type units (Fig. 1e and f) and then further propagated into a three-dimensional (3D) supramolecular structure with one-dimensional (1D) pores that have a diameter of ~ 6.2 Å (Fig. 1b-d). The energy profile provided by density functional theory calculation suggests that *X*-aggregation of tectons can deliver the honeycomb-type hexagonal packing with minimum system energy (Supplementary Figs. 11 and 12). This exquisite packing style can exhibit many advantages, such as practicality, material saving and strong bearing capacity.[20] A space filling diagram viewed along *c*-axis and cross-section further confirmed the "virtual porosity" of the columnar (Supplementary Fig. 10). The total solvent-accessible volume was estimated to be 26.2% of its unit cell volume according to *PLATON* anaylsis.[21]

PCS exhibits AIE behavior, proven by its weak emission in a good solvent (CH_3CN) and enhanced photoluminescence (PL) in a bad solvent (isopropyl ether) (Supplementary Fig. 13). Transparent colorless hexagonal prism shaped single crystals of **PCS**, referred to as **C3**, with blue-green emission can readily be obtained by slow vapor diffusion of diisopropyl ether into its acetonitrile solution (Fig. 2a). Meanwhile, the tunnel structure of **C3** inspired us to investigate whether specific guest vapor molecules can be adsorbed and diffuse directionally inside the crystals which may accompany with vapochromism behavior. Herein, we choose I_2 as the transported guest because its strong fluorescent quenching effect which can be used for monitoring the diffusion; on the other hand radioactive iodine is a public safety hazard therefore effective scavenger is highly desirable.[22] **C3** crystal was placed in vials and then exposed to iodine vapor in a sealed container at room temperature. A few seconds later, staining started from the two capping faces and extended continuously into the central part of the crystals. As seen in Fig. 1i, the face-indexing graphic of **C3** indicates the top and bottom capping face (001) of the hexagonal prism is actually the entrance of the tunnel. After about 2 h, the crystal was entirely colored (Supplementary Fig. S14). Figure 1j and Supplementary Movie S1 records the time-dependent diffusion process from initial to final state accompanied by apparent color change from light yellow to almost black. This phenomenon also excludes the possibility of crystal surface loading. TGA shows the weight capacity of iodine loading was about 18% (Supplementary Fig. S15). When one end of the capping faces of the needle crystal was immersed into

glycerol, the sublimed iodine vapor can only diffusion into the central part of the crystal through the other capping face. The gradually quenched emission started from the unblocked entrance further confirmed the tunnel-type pathway of this assembly from molecular bricks (Figure 1k and Supplementary Movie S2). The result demonstrated that the tunnel structure was quite important for the direction-controllable substance transfer.

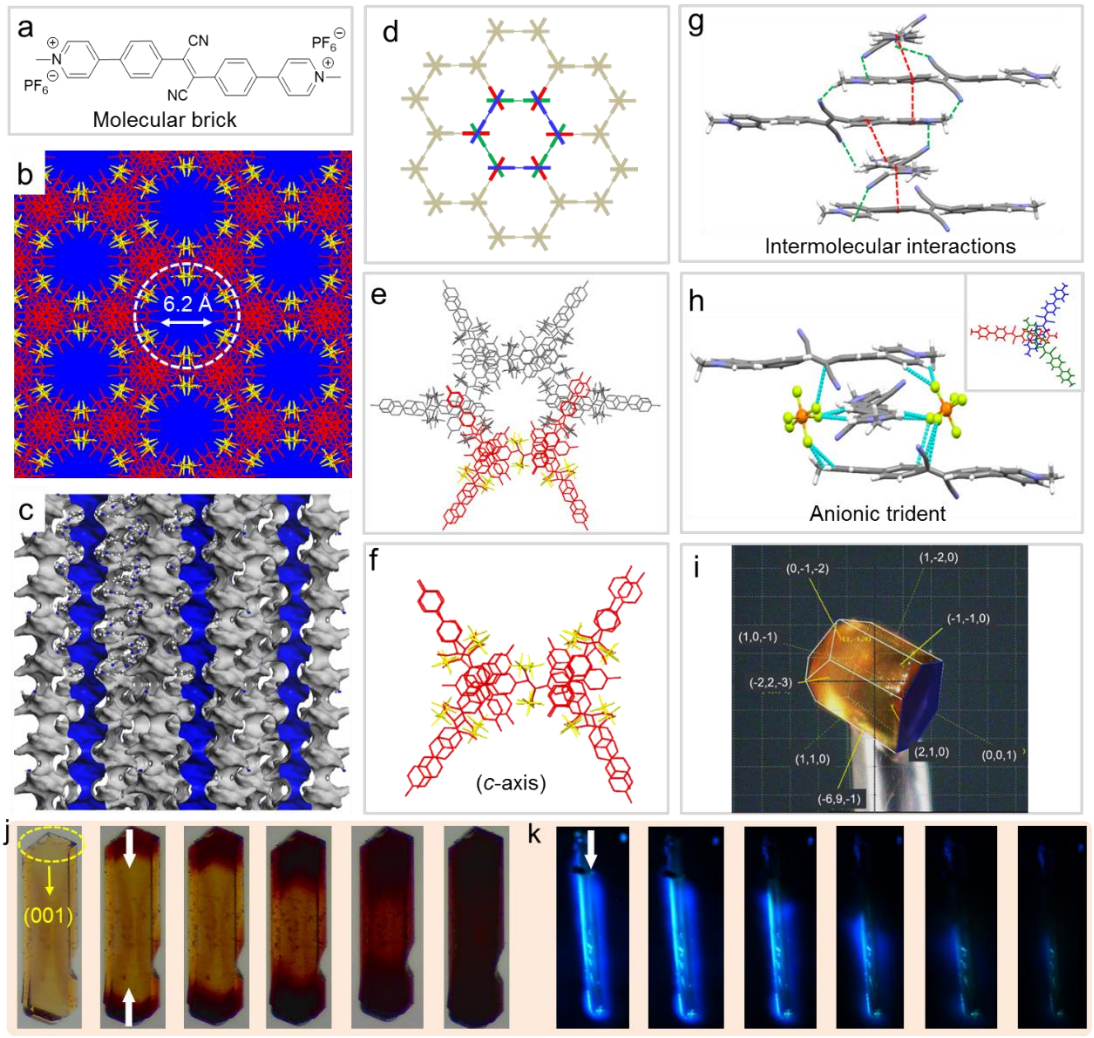

Fig. 1 The formation of porous molecular crystals with tunnel pores. (a) Molecular structure of **PCS**. (b) The honeycomb like tunnel structure viewed along *c*-axis in capped-stick representation. (c) The smoothed solvent accessible surfaces have been added using Materials Studio, and the structures have then been sliced along the *c*-axis. (d) The cartoon representation of the formation of tunnels. (e) Crystal packing along the *c*-axis of the pseudo-hexagonal framework of the tunnel. (f) The minimum repeating units (nano lego) of the crystal lattice along the *c*-axis. (g) Intermolecular interactions. The pink dashed lines indicate C-H...N and π-π interactions. The green dashed line indicated the intermolecular hydrogen bonding with distance less than 2.90 Å. (h) The anionic trident (view along the *a*-axis) that stabilizes the tunnel. The green dashed lines indicate F...π and C-H...F interactions between PF_6^- and **PCS**. PF_6^- in (c), (e) and (g) was omitted for clarity. (i) A crystal of **C3** with face-indexing graphics. The blue hexagon indicates (001) face of the crystal which is also the one of the entrance to the tunnel. (j) **C3** featuring different states of the process of

diffusion in of iodine from initial to final state. Diffusion started progressing from the two capping faces to the central part. (k) Fluorescence images of **C3** at different diffusion states with the bottom capping face immersed into glycerole. Diffusion started progressing from only the top capping face to the central part.

Discrete molecules tend to maximize attractive interactions and leave minimal voids as possible in their crystal packing.[23] Therefore most solvates do not commonly retain their incipient porosity on guest removal, but rather collapse to form a denser phase which may accompany with thermosalient behavior.[24-26] The morphological evolution of one single crystal was monitored under hot stage microscopy (Supplementary Movie S3). The hexagonal prism crystals rapidly crack into small pieces along the longest axis with a gradual color change from transparent colorless to non-transparent light-yellow, some of which can move and even jump out of the visual field under heating (Fig. 2a and b, Supplementary Movie S4). It is found that the crystal dramatically shrinks by 12% volume and turn dark orange around 220 °C (Fig. 2c). The thermosalient behavior occurs as two kinematic effects stages: shrink and shrink followed by hopping. This thermo-responsive mechanical process can not only magnify the underlying molecular-scale mechanism but also lead to an enlightening application for such tunnel structure, such as highly efficient molecular/crystalline actuators and sensors.

TGA profile of crystals with tunnels occupied by solvent molecules (named $\mathbf{C^S}$) showed multistep mass loss to reach a plateau at ca. 280 ºC and this plateau was maintained until decomposition of the material ensues beyond 320 °C (Supplementary Fig. S20). In a DSC profile over a wide temperature range from 5 to 280 ºC, porous $\mathbf{C^S}$ in the first heating process displayed a significant broad endothermic peak around 30-100 °C which was attributed to the loss of solvents (red curve Fig. 2d). This indicates solvents in the voids of $\mathbf{C^S}$ can be removed by heating to 100 °C which also causes the cracking of the crystal. Notably, another single exothermic peak at 220 °C also appeared which was ascribed to a crystalline phase transition.[27] Upon subsequent cooling, neither an exothermic peak nor an endothermic peak appeared (blue curve in Fig. 2d), indicating that the phase transition at 220 °C is irreversible and the new form is thermodynamically more favored than $\mathbf{C^S}$. To further confirm this hypothesis, variable-temperature powered XRD (PXRD) data for $\mathbf{C^S}$ was measured from 50 to 280 °C (Fig. 2e). Its PXRD profile did not show any obvious change below 140 °C. During 140 to 180 °C, broad peaks appear between 10° and 25° suggesting the loss of crystallinity. It should be noted that the PXRD pattern exhibited a sharp and strong peak at $2\theta = 5.80°$ which corresponds to the lattice spacing of d (2,–1,0) plane in the crystal (Fig. 2b). The measured diameter of 15.18 Å of the pore is nearly the same as the calculated layer distance from the Bragg equation (Supplementary Fig. S16), which can be assigning the peak at $2\theta = 5.80°$ relating to the existence of pores. Thus, the unchanged sharp peak at $2\theta = 5.80°$ indicates that the persistence of tunnel structure up to 180 °C. The retained open pore structure even after the removal of the solvents demonstrates the high thermal stability of the porous structure. Upon further heating to 220 °C the PXRD profile changed abruptly and irreversibly with new peaks observed, affording a new crystalline phase.

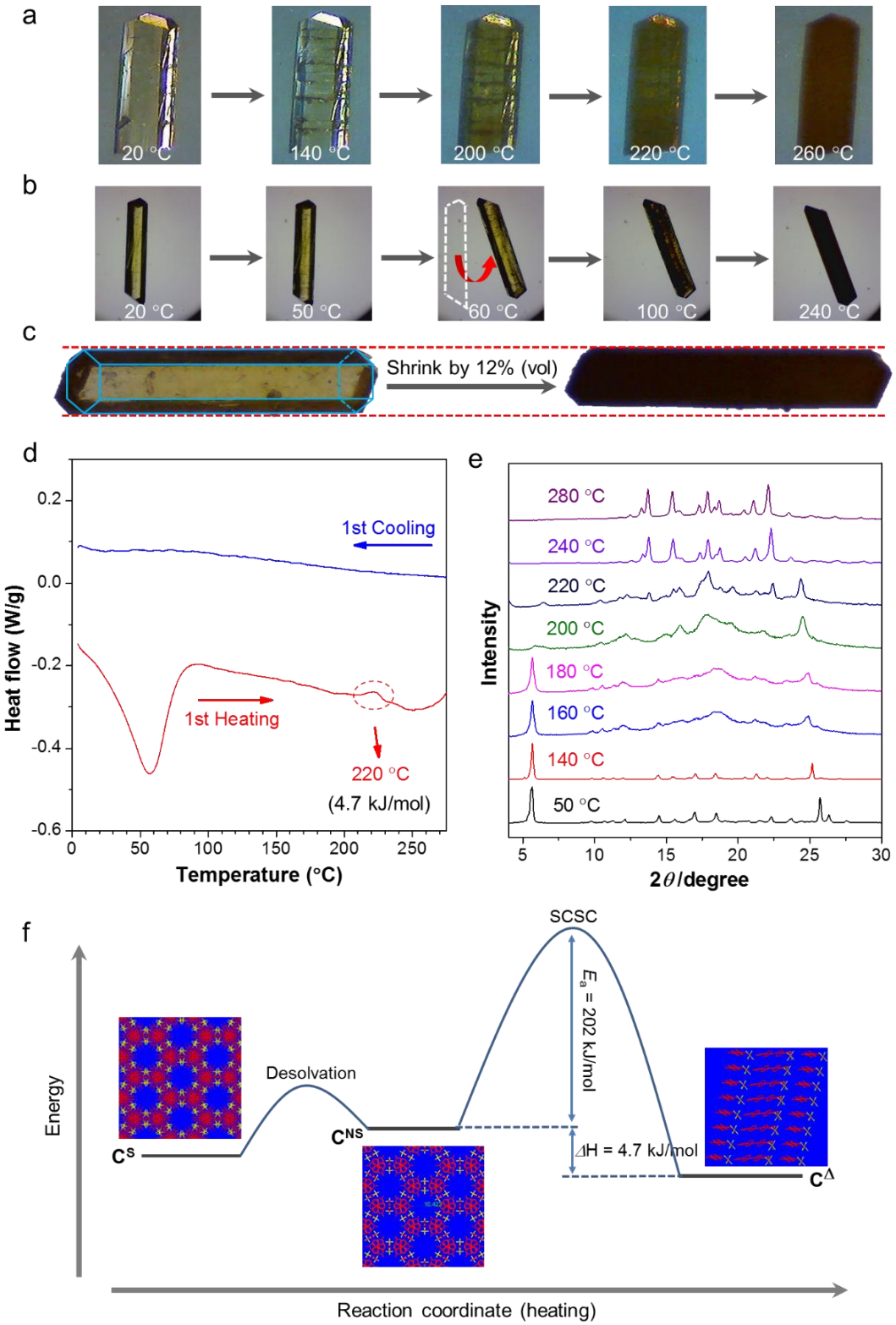

Fig. 2 Thermosalient behavior and multistage polymorphic SCSC phase transformations upon heating. (a) Morphology and colors of single crystals of $\mathbf{C}^{\mathbf{S}}$ that were heated. (b) The crystal jumping behavior of $\mathbf{C}^{\mathbf{S}}$. (c) Crystal morphology shows the volumn shrinking after phase transition. (d) DSC traces of $\mathbf{C}^{\mathbf{S}}$ in the first heating (red curve) and first cooling (blue curve) processes (scan rate = 5 °C min^{-1}). The phase transition temperature is indicated in red dashed circle. Figures were captured from Movie S1 and Movie S2. (e) PXRD profiles of $\mathbf{C}^{\mathbf{S}}$ measured at different temperatures upon

heating. (f) An energy diagram for the heating process. Energy levels were estimated on the basis of the DSC profiles. Inserted are wireframe representations of the crystal-packing diagrams of $\mathbf{C^S}$, $\mathbf{C^{NS}}$ and $\mathbf{C^{\Delta}}$. E_a: Activation energy. $\mathbf{C^S}$ = Solvated porous crystal. $\mathbf{C^{NS}}$ = Non-solvated porous crystal. $\mathbf{C^{\Delta}}$ = Nonporous crystal.

Although under high temperature perturbations, organic crystals are generally fragile to be eligible for single crystal analysis, **PCS** is thermostable in that respect. There was almost no loss of crystallinity for **PCS** after desolvation at 80 °C for 15 h under vacuum. TGA confirms the absence of solvent in the desolvated crystal (Supplementary Fig. S17). The XRD pattern of the desolvated sample was consistent with that of $\mathbf{C^S}$ which confirms the preserved structure (Supplementary Fig. S18). We have also able to resolve the desolvated crystal structure ($\mathbf{C^{NS}}$) which further confirms the intermolecular interactions can survive during crystal evacuation to yield robust structure with pores (Fig. 4a). More surprisingly, the crystalline sample can undergo single-crystal-to-single-crystal (SCSC) transitions at 220 °C to its nonporous polymorph ($\mathbf{C^{\Delta}}$) which also has enough quality for single crystal XRD analysis. This provides us concrete transition information at molecular level. The packing modes of **PCS** molecules in $\mathbf{C^{\Delta}}$ and $\mathbf{C^S}$ changes from *X*-style to *J*-style although their molecular conformations are similar (Supplementary Fig. S19). **PCS** molecules in $\mathbf{C^{\Delta}}$ were connected by infinite intermolecular π-π stacking between adjacent molecules and reoriented in slip-stack with a slip angle of ≈ 35° (Supplementary Fig. S20). The shrink of the crystal volume indicates the packing in $\mathbf{C^{\Delta}}$ is denser than that in $\mathbf{C^S}$. The total solvent-accessible volume of $\mathbf{C^{\Delta}}$ was estimated to be 0% of its unit cell volume at the same condiation as that for $\mathbf{C^S}$ according to *PLATON* anaylsis. As shown in Supplementary Movie S5 and Supplementary Fig. S21, the closed tunnel after SCSC transition was also proven by the blocked diffusion of I_2 into the $\mathbf{C^{\Delta}}$ crystal.

Based on the DSC and TGA profiles, a possible energy diagram for the overall crystalline transformation was proposed. It is suggested that kinetically stable $\mathbf{C^S}$ consecutively undergoes polymorphic transition to the solvent-free $\mathbf{C^{NS}}$ and then nonporous thermodynamic $\mathbf{C^{\Delta}}$. The solvents releasing from $\mathbf{C^S}$ to $\mathbf{C^{NS}}$ likely requires only a very small activation energy, as evidenced by the TGA profile of $\mathbf{C^S}$ (Supplementary Fig. S17). By contrast, the DSC result features a single exothermic peak at 220 °C during the transformation of $\mathbf{C^{NS}}$ into $\mathbf{C^{\Delta}}$, for which enthalpy change was evaluated to be 4.7 kJ mol^{-1} (Fig. 3d). DSC analysis with different scan rates revealed that the phase transition temperature varied with the heating rate, proving that it is indeed a case of kinetically irreversible enantiotropic transition. By means of the Kissinger method the activation energy for this process was calculated to be as high as 202 kJ mol^{-1} which confirms the high thermal stability of the tunnel (Supplementary Fig. S22).

Compared with the extended frameworks, the porous molecular crystals formed by exclusively non-covalent bonding has less stable structure and only a few examples of them have been reported to be stable at acidic or basic condition to date. In fact, most of those supramolecular frameworks would collapse after the solvents being removed. However, the desolvated pore (**C3**) showed surprisingly high stability toward both acid (HCl) and base (NaOH). There was no loss of crystallinity, nor any chemical

decomposition, when solid **C3** was soaked in acidic (pH = 1.0) and alkaline (pH = 10) solutions for 1h, as shown by the PXRD (Fig. 3a) and ^{1}H NMR (Supplementary Fig. S23) results. The excellent robustness of the tunnel may be ascribed to the strong structural support of the anionic trident.

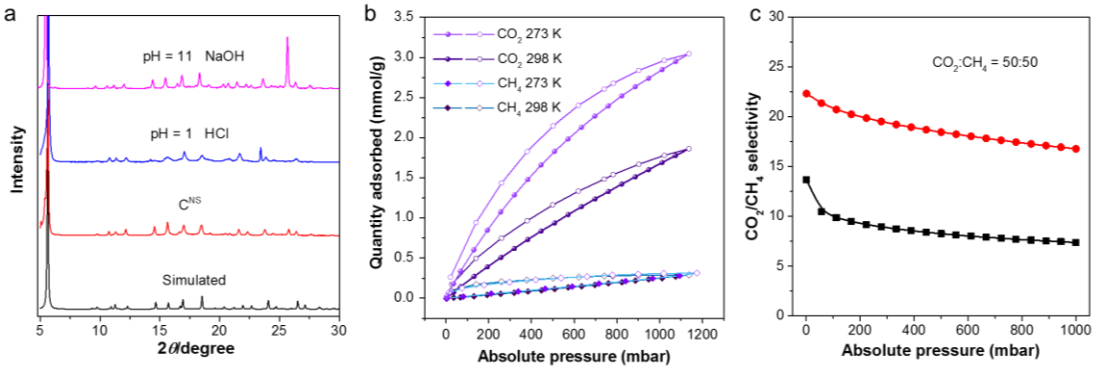

Fig. 3 Stability and selectivity of gas adsorption of the tunnel. (a) PXRD patterns of simulated **C3**, desolvated **C3**, desolvated **C3** in pH = 1 HCl and pH = 10 NaOH aqueous for 20 h. (b) CH_4 (298 K), CH_4 (273 K), CO_2 (298 K) and CO_2 (273 K) adsorption isotherms of $\mathbf{C^{NS}}$. (c) CO_2/N_2 selectivity values of $\mathbf{C^{NS}}$ versus pressure calculated from a 50/50 mixture and applying IAST caculation..

Encouraged by the observed virtual porosity in the activated crystals of $\mathbf{C^{NS}}$, we performed a series of gas sorption measurments using N_2, H_2, Ar, CH_4 and CO_2 (Fig. 5). At 77K, C^{NS} has a modest uptake of N_2 at 0.6 mmol/g at 1 bar, which suggests a Brunauer–Emmett–Teller (BET) surface area at 27 m^2 g^{-1}. Similarly, the H_2 uptake experiment shows a unusual linear isotherm and shows 0.5 mmol/g H_2 was absorbed at 1bar, 77 K. The N_2 and H_2 sorption results are unexpected considering there are channels with size over 6Å presence in the structure, which can normally accomodate N_2 and H_2. On the contrary to other investigated gases, the CO_2 isotherm showed that guest-free $\mathbf{C^{NS}}$ can adsorb a dencent amount of CO_2 at 2.8 mmol/g at 1bar, 273K. The adsorption value at 273 K, 68.1 cm^3 g^{-1} has outperformanced many porous hydrogen-bonds and supramolecular organic frameworks[9,28,29] at 1 bar room temperature. The calculated pore size of 7.5 Å (Supplementary Fig. S25) from the CO_2 isotherm is not far from the value (6.2 A, Fig 1b) obtained from the crystal structure. Ideal adsorbed solution theory (IAST) was used to predict binary 50:50 feed CO_2 and CH_4 mixture adsorption, giving predicted CO_2/CH_4 selectivity at 16.8 (273 K) and 7.4 (298 K), respectively.[30] The absorption enthalpy of 25 kJ mol^{-1} at 273 K for CO_2 ruled out the possibility of chemisorption (Supplementary Fig. S26). Though there are many PF_6^- surrounded the inner circle of the pores, the existing models may not be well-suited for fluorine lined pores such as those of our porous molecular crystal,[31] crystal structure data of $\mathbf{C^{NS}}$ suggests an ultramicropore with 0.6 nm in diameter (Fig. 1b). The highly selective adsorption may be ascribed to the higher quadrupole moment of CO_2 (-1.4×10^{-39} C m^2) than those of N_2 (4.7×10^{-40} C m^2), H_2 (2.2×10^{-40} C m^2) and CH_4 (0), which can thus enhance the electrostatic interactions between CO_2 and the framework, resulting in the increase of CO_2 binding.[32] Chargs on the surface of the pores have prohibite the adsorption of gases such as N_2, H_2 and CH_4, while not affect the uptake of

CO_2 molecules. Similar behaviour has also been observed in other charged channel system.[33]

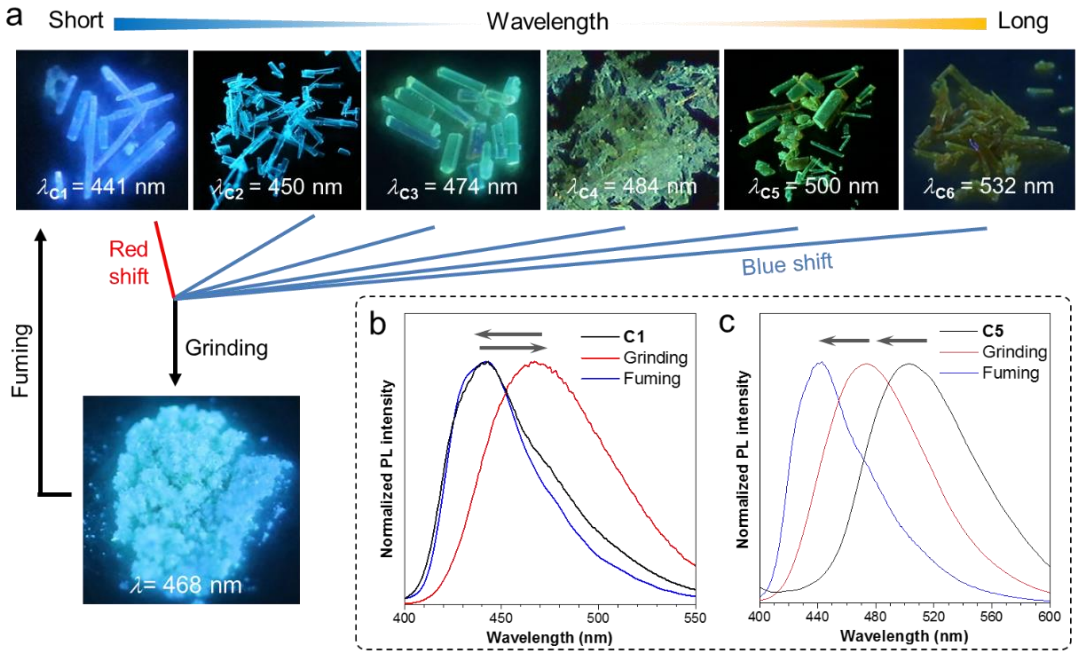

Fig. 4 Visible self-healing porosity transformation upon stimulating. (a) Fluorescence images of **C1**–**C6** and their grinded and further fumed samples. Normalized emission spectra of (b) **C1** and (c) **C5** and their corresponding grinded and fumed spectra.

X-ray crystal analysis reveals that the PF_6^- anions and the methyl groups of **C3** are exposed on the pore surfaces for potential interactions with guest molecules (Fig. 1b). Considering the AIE character of the tecton, these interactions with adsorbents may further leads to responsive fluorescence change.[34] Thanks to the strong crystallization tendency, we obtained crystals under different cultivating conditions and six kinds of crystals named **C1**-**C6** were obtained, with different emission wavelengths ranging from 441 to 532 nm (Fig. 4a). All the six single crystals have the sharp peak at 2θ = 5.80° in their PXRD profile which suggests the existence of pores (Supplementary Fig. S27). However, because of the highly disordered solvents and the resulted in asymmetrical molecular structure, we can only resolve three crystal structures of them: the blue emissive **C1** (441 nm), the aforementioned blue-green emissive **C3** (474 nm) and the green emissive **C5** (500 nm). Simulated PXRD of **C1**, **C3**, and **C5** from the single crystal data show almost identical patterns which means they have very similar crystal packing (Supplementary Fig. S28). This was further confirmed by the same pore along *c*-axis in their crystal structures (Supplementary Fig. S29). TGA of freshly prepared six crystals and ^{1}H NMR spectra of their solution of freshly prepared crystals in DMSO-d_6 indicates the possible included solvents in their voids (Supplementary Figs. S30 and 31). Moreover, crystallographically, one **PCS** molecule interacts with four surrounding molecules; and all these participated molecules adopt twisted conformation with different rotation angles and different distances of intermolecular hydrogen bonds / π-π interactions (Supplementary Fig. S32). Thus, it is assumed that the different emission of six porous structures are caused by the synergy effect of the

variation of intermolecular distances, the conformation change of the methyl groups, and the solvents effects on the exposed PF_6^- ions.

The exclusive non-covalent interactions endow the porous molecular crystals with dynamic behavior. Grinding can destruct the highly ordered crystalline porous structure and result the characteristic peak in PXRD pattern disappear (Supplementary Fig. S26). After grinding, the emission of all samples shifted to 468 nm which was ascribed to the stable nonporous state $\mathbf{C}^{\mathbf{\Delta}}$. Notably, for **C1,** the emission color red-shifted after grinding, while the emission of **C5** blue-shifted after grinding (Fig. 4b and c). Further exposing the nonporous powder with dichloromethane or acetonitrile vapors, the recovery of reflection peaks in the PXRD patterns assignable to **C1** was observed, indicated grinded samples could self-heal to regain its parental structure (Supplementary Fig. S26). For grinded **C1**, its emission return to the initial state (441 nm), while for grinded **C5**, fuming induced further blue-shifting the emission to 441 nm (Fig. 4b and c and Supplementary Fig. S33). This means after recrystallization **C1** should be the energy-minimal structure in solid state. Similar mechanochromic luminescent was observed for the other three porous crystals **C2**, **C4** and **C6** (Supplementary Fig. S34). Therefore, we are able to realize on-off-on switching of porosity through grinding and vapor-fuming, simultaneously accompanied by hypochromatic or bathochromatic shifts. The self-healing porosity transformations are easily visualized, making this tunnel structure holds promise for applications such as chemical sensors, data recording and other smart materials.

Discussion

In summary, we have successfully assembled a robust porous molecular crystal through a synergy arrangement of strong anionic trident and intermolecular π-π interactions from a geometrically simple molecule. Upon thermal treatment, the formed nano-tunnel crystals go through multistage polymorphic SCSC phase transformations accompanied by thermosalient effect. The nano-tunnel crystal exhibit exceptional chemical stability in concentrated HCl and NaOH aqueous solutions, which is rarely been seen in supramolecular organic frameworks. Aggregation-induced emission joins with the adaptive pores render the crystals with responsive fluorescent change from blue to yellow and visible self-healing porosity transformation upon being stimulated. Furthermore, the desolvated pores exhibit highly selective CO_2 adsorption at ambient temperature. This scarce two-armed organic building unit in combination with anionic-facilitated strategy opens a new vista in construction of functional porous molecular frameworks.

Methods

Preparation of the single crystals. The single crystal of **PCS**-I was obtained by slow evaporation of a saturated solution in methanol at room temperature for one week. The preparations of single crystals of **C1** and **C2** are similar to that of **PCS**-I but with acetone instead of methanol. The single crystals of **C3** and **C5** suitable for X-ray diffraction analysis were grown at room temperature for 2-3 days by slow vapor diffusion of diisopropyl ether into their acetonitrile solution. The single crystal of **C4** was grown by slow vapor diffusion of *n*-pentane into their acetone solution. The

preparation of single crystal of **C6** is similar to that of **PCS**-I, but with acetonitrile instead of methanol and meanwhile with addition of a drop of ethanol.

Gas Sorption Analysis. All samples were tested with gases of the following purities: hydrogen (99.9995%-BOC gases), carbon dioxide (SCF grade-BOC gases) and methane (ultrahigh purity-BOC). Surface areas and pore size distributions were measured by nitrogen adsorption and desorption at 77.3 K using a Micromeritics ASAP 2020 volumetric adsorption analyzer. Samples were degassed at offline at 80 °C for 15 h under vacuum (10^{-5} bar) before analysis, followed by degassing on the analysis port under vacuum, also at 80 °C. Both methane and carbon dioxide isotherms were measured at ambient temperature, while argon at 87 K and hydrogen were measured at 77.3 K (liquid N_2), using a Micromeritics 2420 volumetric adsorption analyzer using the same degassing procedure.

Data availability

The data that support the findings of this study are available from the authors on reasonable request, see author contributions for specific data sets. The X-ray crystallographic coordinates for the structures reported in this article have been deposited at the Cambridge Crystallographic Data Centre (CCDC). These data can be obtained free of charge from The Cambridge Crystallographic Data Centre via www.ccdc.cam.ac.uk/data_request/cif.

Acknowledgements

This work was supported by the National Science Foundation of China (21788102, 81372274, 81501591 and 8141101080), the Research Grants Council of Hong Kong (16308016, C6009-17G and 16305618 and 16304819), the Innovation and Technology Commission (ITC-CNERC14SC01) and the Science and Technology Plan of Shenzhen (JCYJ20160229205601482, JCYJ20170818113602462 and JCYJ20170818113348852).

Author contributions

P.W. and B.T. conceived and designed the experiments. P.W. synthesized and characterized the compounds. P.W. performed the experiments. Z.Z., J.G. and other authors were all involved in the analyses and interpretation of data. J.Z., H.H.Y.S. and I.D.W. did the crystal analysis. P.W. and J.W.Y.L. wrote the manuscript with comments from all authors.

Additional information

Supplementary information is available in the online version of the paper. Reprints and permissions information is available online at www.nature.com/reprints. Correspondence and requests for materials should be addressed to B.Z.T.

Competing interests

The authors declare no competing interests.

Reference

1 Bezzu, C. G., Helliwell, M., Warren, J. E., Allan, D. R. & McKeown, N. B. Heme-like coordination chemistry within nanoporous molecular crystals. *Science* **327**, 1627-1630 (2010).

2 Beaudoin, D., Maris, T. & Wuest, J. D. Constructing monocrystalline covalent organic networks by polymerization. *Nat. Chem.* **5**, 830-834 (2013).

3 Barrer, R. M. & Shanson, V. H. Dianin's compound as a zeolitic sorbent. *J. Chem. Soc., Chem. Commun.*, 333-334 (1976).

4 Mastalerz, M. & Oppel, I. M. Rational construction of an extrinsic porous molecular crystal with an extraordinary high specific surface area. *Angew. Chem. Int. Ed.* **51**, 5252-5255 (2012).

5 McKeown, N. B. Nanoporous molecular crystals. *J. Mater. Chem.* **20**, 10588-10597 (2010).

6 Sozzani, P., Bracco, S., Comotti, A., Ferretti, L. & Simonutti, R. Methane and Carbon Dioxide Storage in a Porous van der Waals Crystal. *Angew. Chem. Int. Ed.* **44**, 1816-1820 (2005).

7 Tian, J., Thallapally, P. K. & McGrail, B. P. Porous organic molecular materials. *CrystEngComm* **14**, 1909-1919 (2012).

8 Lü, J. & Cao, R. Porous organic molecular frameworks with extrinsic porosity: A platform for carbon storage and separation. *Angew. Chem. Int. Ed.* **55**, 9474-9480 (2016).

9 Yang, W. *et al.* Exceptional thermal stability in a supramolecular organic framework: porosity and gas storage. *J. Am. Chem. Soc.* **132**, 14457-14469 (2010).

10 Cooper, A. I. Nanoporous organics enter the cage age. *Angew. Chem. Int. Ed.* **50**, 996-998 (2011).

11 Atwood, J. L., Barbour, L. J. & Jerga, A. Storage of methane and freon by interstitial van der Waals confinement. *Science* **296**, 2367-2369 (2002).

12 Evans, J. D. *et al.* Computational identification of organic porous molecular crystals. *CrystEngComm* **18**, 4133-4141 (2016).

13 Xing, G., Yan, T., Das, S., Ben, T. & Qiu, S. Synthesis of crystalline porous organic salts with high proton conductivity. *Angew. Chem. Int. Ed.* **57**, 5345-5349 (2018).

14 Zhang, K.-D. *et al.* Toward a single-layer two-dimensional honeycomb supramolecular organic framework in water. *J. Am. Chem. Soc.* **135**, 17913-17918 (2013).

15 Hisaki, I., Xin, C., Takahashi, K. & Nakamura, T. Designing Hydrogen-Bonded Organic Frameworks (HOFs) with Permanent Porosity. *Angew. Chem. Int. Ed.* **58**, 11160-11170 (2019).

16 Lin, R.-B. *et al.* Multifunctional porous hydrogen-bonded organic framework materials. *Chem. Soc. Rev.* **48**, 1362-1389 (2019).

17 Yamamoto, A., Hamada, T., Hisaki, I., Miyata, M. & Tohnai, N. Dynamically

Deformable Cube-like Hydrogen-Bonding Networks in Water-Responsive Diamondoid Porous Organic Salts. *Angew. Chem. Int. Ed.* **52**, 1709-1712 (2013).

18 Mei, J., Leung, N. L., Kwok, R. T., Lam, J. W. & Tang, B. Z. Aggregation-induced emission: together we shine, united we soar! *Chem. Rev.* **115**, 11718-11940 (2015).

19 Zhang, M. *et al.* Two-dimensional metal–organic framework with wide channels and responsive turn-on fluorescence for the chemical sensing of volatile organic compounds. *J. Am. Chem. Soc.* **136**, 7241-7244 (2014).

20 Kataoka, K. *et al.* A molecular-sized tunnel-porous crystal with a ratchet gear structure and its one-way guest-molecule transportation property. *Nanoscale* **5**, 1298-1300 (2013).

21 Spek, A. PLATON, a multipurpose crystallographic tool (Version 10M). *Utrecht University, Utrecht, The Netherlands* (2003).

22 Riley, B. J., Vienna, J. D., Strachan, D. M., McCloy, J. S. & Jerden Jr, J. L. Materials and processes for the effective capture and immobilization of radioiodine: A review. *J. Nucl. Mater.* **470**, 307-326 (2016).

23 Dunitz, J. D. & Gavezzotti, A. How molecules stick together in organic crystals: weak intermolecular interactions. *Chem. Soc. Rev.* **38**, 2622-2633 (2009).

24 Barbour, L. J. Crystal porosity and the burden of proof. *Chem. Commun.*, 1163-1168 (2006).

25 Sahoo, S. C., Panda, M. K., Nath, N. K. & Naumov, P. e. Biomimetic crystalline actuators: structure–kinematic aspects of the self-actuation and motility of thermosalient crystals. *J. Am. Chem. Soc.* **135**, 12241-12251 (2013).

26 Brunet, P., Simard, M. & Wuest, J. D. Molecular tectonics. Porous hydrogen-bonded networks with unprecedented structural integrity. *J. Am. Chem. Soc.* **119**, 2737-2738 (1997).

27 Ge, C. *et al.* Visualization of Single-Crystal-to-Single-Crystal Phase Transition of Luminescent Molecular Polymorphs. *J. Phy. Chem. C* **122**, 15744-15752 (2018).

28 Li, P. *et al.* A rod-packing microporous hydrogen-bonded organic framework for highly selective separation of C2H2/CO2 at room temperature. *Angew. Chem. Int. Ed.* **54**, 574-577 (2015).

29 Lü, J. *et al.* A robust binary supramolecular organic framework (SOF) with high CO2 adsorption and selectivity. *J. Am. Chem. Soc.* **136**, 12828-12831 (2014).

30 Lee, S., Lee, J. H. & Kim, J. User-friendly graphical user interface software for ideal adsorbed solution theory calculations. *Korean J. Chem. Eng.* **35**, 214-221 (2018).

31 Chen, T.-H. *et al.* Thermally robust and porous noncovalent organic framework with high affinity for fluorocarbons and CFCs. *Nat. Commun.* **5**, 1-8 (2014).

32 Luo, X.-Z. *et al.* A microporous hydrogen-bonded organic framework: exceptional stability and highly selective adsorption of gas and liquid. *J. Am. Chem. Soc.* **135**, 11684-11687 (2013).

33 Xing, G. *et al.* A double helix of opposite charges to form channels with unique CO 2 selectivity and dynamics. *Chem. Sci.* **10**, 730-736 (2019).

34 Wang, B. *et al.* A Microporous Hydrogen-Bonded Organic Framework for Highly Efficient Turn-Up Fluorescent Sensing of Aniline. *J. Am. Chem. Soc.* DOI: 10.1021/jacs.0c05277 (2020).